Scattering of topological kink-antikink states in bilayer graphene

Nassima Benchtaber,[1] David Sánchez,[1, 2] and Llorenç Serra[1, 2]

[1]*Institute of Interdisciplinary Physics and Complex Systems IFISC (CSIC-UIB), E-07122 Palma, Spain*
[2]*Department of Physics, University of the Balearic Islands, E-07122 Palma, Spain*

Gapped bilayer graphene can support the presence of intragap states due to kink gate potentials applied to the graphene layers. Electrons in these states display valley-momentum locking, which makes them attractive for topological valleytronics. Here, we show that kink-antikink local potentials enable modulated scattering of topological currents. We find that the kink-antikink coupling leads to anomalous steps in the junction conductance. Further, when the constriction detaches from the propagating modes, forming a loop, the conductance reveals the system energy spectrum. Remarkably, these kink-antikink devices can also work as valley filters with tiny magnetic fields.

I. INTRODUCTION

For many years, there has been considerable interest in providing with reliable platforms that can create, manipulate and detect qubits. Eventually, these quantum information processing tasks are to be supplemented with protected communication channels to transmit quantum states between distant sites. Graphene has emerged as an excellent candidate in scalable solid-state architectures due to its ultra long decoherence times for spin qubits and its ability to host additional isospin (valley) degrees of freedom[1–3]. These emerge as the K and K' points from the Dirac cones in the reciprocal space of the graphene hexagonal lattice.

However, pristine graphene lacks a bandgap, which handicaps potential applications of this material for nanoelectronics. This circumstance can be surpassed with the employment of two graphene sheets (hereafter, bilayer graphene or BLG)[4,5]. Interlayer coupling in a Bernal stacking structure (common also to graphite) generates a huge band splitting of the order of 380 meV, although two bands still remain degenerate at the neutrality point. Further application of a perpendicular electric field creating a potential difference between the two layers finally lifts the electronic degeneracy[6,7]. The gap thus opened can now be used to design tunnel barriers and quantum point contacts[8,9]. Unlike monolayer point contacts that are fabricated by etching[10,11] and show trapped states due to edge roughness, BLG quantum wires display clear conductance quantization steps. Further, if two of these barriers are connected in a series the device works as a quantum dot[12–15]. Therefore, robust spin or valley qubits can form in BLG dots showing a discrete spectrum.

An even more exciting possibility arises in BLG systems. When the perpendicular electric field becomes inhomogeneous by changing its sign in different regions of the BLG, the domain wall separating the two opposite fields holds topological states propagating next to the wall (edge states)[16,17]. These types of domain wall and propagating states are known as kink and kink states, respectively. The topological character originates from the field induced band inversion and confinement. Interestingly, the valley index remains a good quantum number[18] and as a consequence the kink states become chiral with different valleys traveling in opposite directions along the kink[19]. Crucially, such propagating states exist at zero magnetic field and for vanishing spin-orbit coupling. Hence, if electrons are injected from the side into a straight kink using a small dc bias, the output flux becomes valley polarized. If the structure is built zero dimensional like a dot, the bound states are valley degenerate but chiral. These topological states can even show Luttinger behavior[20] or become massless Dirac modes[21] in the presence of interactions or periodic potentials, respectively.

The challenge then is how to probe and manipulate these unique kink states. This can be achieved with pairs of gates whose voltage is tuned independently in both the top and bottom layers[22,23]. Experimentally, a conductance of $4e^2/h$ is observed, which demonstrates the presence of two current-carrying spin-degenerate valley-polarized modes. Alternate combinations of dual gates can be implemented for guiding these modes in valley valves and beam splitters[24,25]. However, signatures of disorder are detected, inducing backscattering and intervalley mixing. What is needed is a controlled source of backscattering that would allow to shape ballistic beam splitters for, e.g., topological valleytronic interferometry[26]. Here, we show that this is possible with a careful distribution of top/bottom gate pairs, enabling the formation of a lateral constriction over *two* parallel kinks, as sketched in Fig. 1a. The two kinks have symmetric changes in the field polarity and opposite propagation directions for a given valley, thus one kink being the antikink of the other[16,17]. We below demonstrate that a kink-antikink constriction is able to modulate the transmission electrostatically, what paves the way for the fabrication of topological quantum point contacts and wires.

Importantly, the setup can be slightly rearranged to also furnish bound states when the kink-antikink constriction (Fig. 1b) transforms into a side loop (Fig. 1c). Previous works on similar BLG islands assumed a sharp-potential kink[27] or infinite-mass boundary conditions[28] that create rings exhibiting Aharonov-Bohm energy levels. However, these are closed systems and as such their properties would be difficult to examine in an experiment. In contrast, our loops are weakly coupled to the
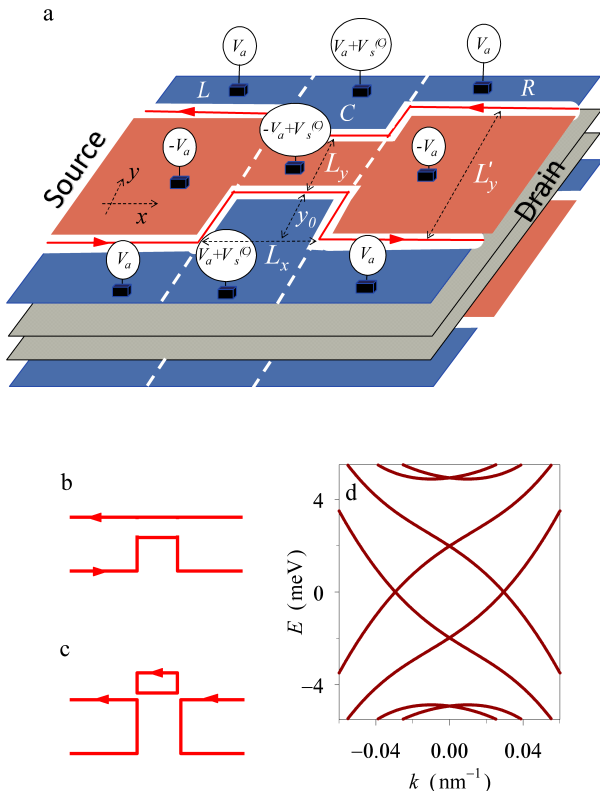
FIG. 1. (a) Schematic of a bilayer graphene kink-antikink system with lead regions (L and R) and a central scatterer (C). The electric field direction on the graphene layers (gray sheets) is controlled by the voltages applied to the nine top and bottom gates (blue and orange regions). The values of the V_a applied potentials to the lower gates (not shown) are reversed with respect to the top gates. The field inversion between the blue and orange regions creates an interface (white region) where topological modes emerge. Additionally, a voltage $V_s^{(C)}$ is applied only to the central region. Red lines represent these propagating topological modes for the valley K. K' modes are obtained by reversing the arrows. Current is generated from the left (source) terminal to the right (drain) terminal. Dimensions and position of the central scatterer are given by L_x, L_y and y_0, while the asymptotic separation of the two kinks is L'_y. (b,c) Selected configurations representing a constriction (b) and a side loop (c), the latter formed when $y_0 > L'_y$. (d) Energy bands of a translationally invariant kink-antikink wire of width $L'_y = 300$ nm, kink potential height $V_a = 10$ meV and potential smoothness $s = 38$ nm. Each band is fourfold degenerate (spin and valley) in the absence of magnetic fields.

external (side) kinks, topological as well. We show that the measured conductance peaks correlate with the system levels and the setup is therefore most suitable for doing spectroscopy of chiral bound states.

Let us discuss in more detail our proposal, as illustrated in Fig. 1a, and highlight our main findings. The system consists of a BLG with the same gate distribution in both the upper and lower graphene layers (gray

sheets). The applied potentials to the lower gates, not shown in Fig. 1a, reverse the values for V_a with respect to the top gates but keep the same value for $V_s^{(C)}$, as detailed below in Sec. II. The changes in electric field orientation occur in the white interfaces defining, respectively, the topological kink and antikink that form the quasi-one dimensional (1D) propagating channels. The arrows in Fig. 1a qualitatively indicate electron propagation for a given valley on the BLG planes when the kink and antikink are well separated. x is the transport direction, the edge states are confined along y and the direction perpendicular to the graphene layers is denoted with z (not shown here). Electronic motion is determined by chirality due to valley-momentum locking (we only depict states from valley K). A narrow central constriction allows for a controlled transmission of the injected beams (see Fig. 1b). We find *anomalous* steps of the conductance as the central potential is varied. If the constriction detaches from the left and right channels, a loop then forms (Fig. 1c) and the conductance now displays *resonant* peaks, their location giving information about the energy levels inside the loop. Altogether, the structure is a remarkable playground for electrical transport studies of both propagating and localized topological valley states.

II. MODEL

We use an effective eight-component model, valid for low energies near the Dirac points of the BLG crystalline band structure. The Hamiltonian reads[4,5]

$$H = v_F \left(p_x - \hbar \frac{y}{l_z^2} \right) \tau_z \sigma_x + v_F \, p_y \sigma_y$$
$$+ \frac{t}{2} \left(\lambda_x \sigma_x + \lambda_y \sigma_y \right) + V_s + V_a \, \lambda_z \, , \quad (1)$$

with three characteristic pseudospins (valley τ_{xyz}, sublattice σ_{xyz} and layer λ_{xyz}) described by corresponding Pauli matrices while p_x and p_y are momentum operators. Two of the model parameters are intrinsic of BLG, namely, the graphene Fermi velocity $\hbar v_F = 660$ meV nm and the interlayer coupling $t = 380$ meV. Then, $l_z = \sqrt{\hbar/eB}$ is the magnetic length for an external magnetic field B whereas V_s and V_a are respectively the symmetric and asymmetric potentials applied to the layers. For uniform potentials, V_s is just a global energy shift while V_a is a displacement energy that opens a gap in the BLG spectrum.

We first discuss the spectrum that arises from Eq. (1) for a kink-antikink system at $B = 0$ and $V_s = 0$. Whenever $V_a = V_a(y)$ changes its sign the gap is inverted and as a consequence four topological states per valley appear at each kink[16,17]. These correspond to the branches seen around zero energy in Fig. 1d. The states above $E = 4.2$ meV are extended states that do not remain attached to the kinks in contrast to the topological states. Further, the energy bands in Fig. 1d are not bounded

either from below or from above since Eq. (1) describes Dirac fermions. We also note that H is both valley diagonal (so that each valley can be independently treated in a four-component subspace) and diagonal in the real spin basis. However, whereas all states are hereafter degenerate for spins up and down, the spectrum is not valley degenerate but obeys $E(k, \tau_z \to 1) = E(-k, \tau_z \to -1)$ due to time reversal symmetry. As a consequence, kink-antikink currents are valley unpolarized. Later, we will remark that a magnetic field breaks time reversal symmetry and thus valley polarizations can be observed in the measured conductance.

In our calculations, the kink potentials vary smoothly in y by means of a diffusivity s (see App. A for details of the potential modeling). This smoothness becomes important when the kink-antikink separation is small, i.e., the constriction in Fig. 1b or the loop in Fig. 1c. Then, s couples the kink states running on the two sides, a mechanism that is eventually responsible for the transmission modulation. Along the transport direction x, the potential interfaces are considered sharp. This assumption is well justified since the mode wavelength λ is much larger than the characteristic length l_a for inversion of the static potentials. Electrostatic modeling in bilayer graphene[22,23] yields an estimate $l_a < 50$ nm, while in our calculations we typically have $\lambda \gtrsim 300$ nm.

We next consider the inhomogenous situation with L, C and R regions along the transport direction x, sketched in Fig. 1a. The distribution of applied potentials is seen in Fig. 1a for the top layer. Gates on the bottom layer have reversed V_a and the same central shift $V_s^{(C)}$. We solve the scattering problem in the presence of either the constriction or the loop using complex band structure methods[29,30]. This technique is especially well suited to describe piecewise homogenous potentials in topological systems. For each region $a = L, C, R$ in Fig. 1a, a large set of complex wavenumbers and eigenstates $\{k^{(a)}, \phi_k^{(a)}\}$ is determined by exact diagonalization[31]. These sets of solutions are then properly matched at the interfaces between central (C) and side regions (L, R). The ensuing linear system of equations yields the transmission amplitudes $t_{n'n}$ from input mode n to output mode n'. The electric conductance is then determined by the two-terminal formula $G = (2e^2/h) \sum_{nn'} |t_{n'n}|^2$, where spin degeneracy is already taken into account and we assume zero temperature (the experiments in Ref. 8 are done at a very low temperature of 1.7 K). The set of complex wavenumbers and wavefunctions of each region is obtained with a finite difference discretization of a 1D equation depending only on y since the x dependence disappears thanks to the homogeneity of each region along the transport direction. This 1D character enables an accurate numerical resolution for large numbers of y grid points, while no grid in x is needed.

The use of grid discretization methods for Dirac-like problems leads to the infamous Fermion doubling problem[32–34], which introduces spurious replica states. These are characterized by very short wavelength oscil-lations, strongly fluctuating from one grid point to the next. Similar replicas are obtained in our approach when calculating the complex band structure of each region $\{k^{(a)}, \phi_k^{(a)}\}$. We filter out the replicas by coarse graining, performing an average with the right or left neighboring point and neglecting those states whose norm is affected by coarse graining. For dense grids, we easily arrive at an unambiguous identification of the physical states, which need to be smooth on the grid by definition. Thus, the Fermion doubling problem does not affect the linear system that determines the conductance since G is based only on the sets of previously filtered solutions $\{k^{(a)}, \phi_k^{(a)}\}$ and no further spatial grid is required near the interfaces.

III. RESULTS

We study two systems formed with the gate distribution and geometry depicted in Fig. 1a: (i) when $y_0 < L'_y$ propagating modes can exist within the central area and a quantum point contact behavior is expected (Fig. 1b); (ii) when $y_0 > L'_y$ a loop detaches from the left and right leads (Fig. 1c) and we will consequently find quantum resonance effects. In both devices, a key parameter is the symmetric potential $V_s^{(C)}$ in the central region, which acts as an effective local probe allowing energy spectroscopy of the constriction.

A. Quantum point contacts

We first present results for the narrow point contact with a kink-antikink separation of 100 nm. This value is compatible with the width of presently available BLG point contacts[8,9]. We set the kink diffusivity to $s = 40$ nm, which is taken from the electric potential distribution in dual split gate BLG devices[22,23], and assume an almost vanishing Fermi energy $E = 0.02$ meV, close to the charge neutrality point.

The conductance for a $1\,\mu$m-long constriction (hereafter the wire) as a function of the central potential is shown in Fig. 2a. We observe that G is strongly suppressed around $V_s^{(C)} = 0$ (region A). This is in principle a surprise since the presence of the edge states at $E = 0$ in Fig. 1d would imply a fully transparent constriction. However, when we plot in Fig. 2b the wire band structure we notice that the topological bands display an absolute gap (for any k) in region A (details of this gap are discussed in App. B). The kink potentials in the constriction couple the edge states, leading to an almost complete backscattering and hence a reduction of the conductance. G does not reach zero because the electrons can traverse the constriction by tunnel effect, which yields in any case a tiny value for G. Then, as $V_s^{(C)}$ increases the energy exceeds the gap and we find in region B two propagating states with positive velocity, per valley and spin. It fol-
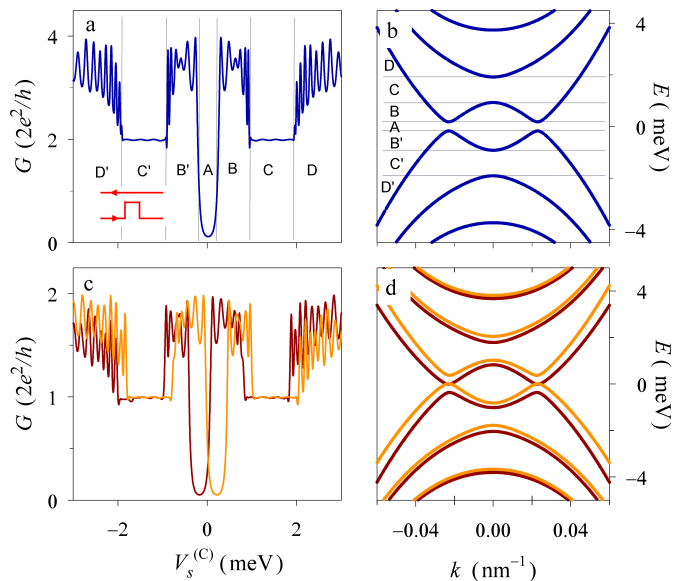
FIG. 2. Results for a narrow constriction (inset in panel a) with $L_y = 100\,$nm, $y_0 = 200\,$nm and a Fermi energy $E = 0.02\,$meV. (a) Conductance for $L_x = 1\,\mu$m as a function of the central potential $V_s^{(C)}$. (b) Energy bands for a kink-antikink wire having the same parameters of the constriction. The capital letters and horizontal lines indicate the correspondence with the conductance ranges of panel a. (c,d) Same as panels a and b, respectively, with a magnetic field of $B = 50\,$mT. The two colors mark the two different valleys.
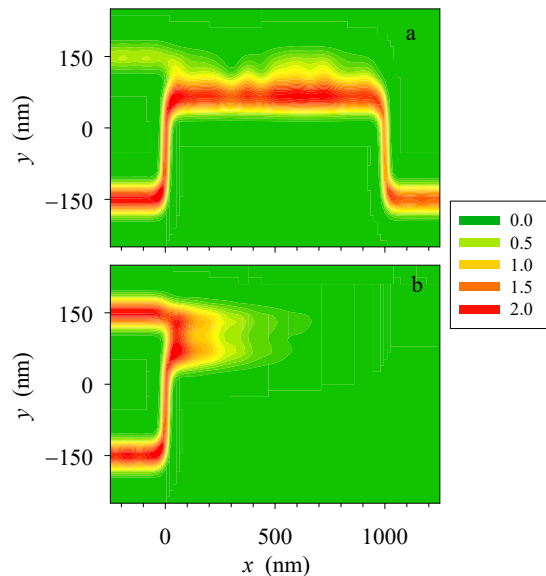

FIG. 3. Density distribution, in arbitrary units, corresponding to the conductance curves of Fig. 2c. Panels a and b are for the two different valleys K and K', respectively. Parameters: $L_x = 1000$ nm, $L_y = 100$ nm, $L_y' = 300$ nm, $y_0 = 200$ nm, $B = 50$ mT, $E = 0.02$ meV and $V_s^{(C)} = 0.2$ meV.

lows that G quickly reaches the quantized value of $8e^2/h$. If $V_s^{(C)}$ is further enhanced we enter region C, where a single mode is only allowed, thus bringing G down to an anomalous step of $4e^2/h$. Finally, larger values of $V_s^{(C)}$ approach us into region D, where another mode starts to contribute and G grows again. The oscillations seen in Fig. 2a are due to quantum interference of several modes coexisting in the wire. We can thus conclude that there is a remarkable correspondence between G and the wire energy bands. In fact, the particle-hole symmetry of Fig. 2b implies that $G(V_s^{(C)}) = G(-V_s^{(C)})$, as found in Fig. 2a. We also point out that for nonzero temperatures the conductance curves will be thermal smeared.

A small magnetic field, in the mT range, suffices to yield large effects on the constriction conductance even if the valley splitting of the energy bands is small (Fig. 2c). Here, we choose to separately display each valley contribution to the conductance. Accordingly, the scale of G reduces a factor $2e^2/h$ as compared with Fig. 2a. We find that the conductance shifts in opposite directions for the two valleys $\tau_z \to \pm 1$, making it possible the creation of highly polarized valley currents, where one valley component is essentially blocked while the other is transmitted. The valley split bands are shown in Fig. 2d. This behavior can be also seen with a single kink due to valley-momentum locking. However, if

we wish to invert the current valley polarization with a kink we would need to revert the extended lateral gates defining the kink whereas Fig. 2c shows the interesting possibility of switching the valley polarization by simply changing $V_s^{(C)}$, leaving both the lateral gates defining the kinks and the magnetic field fixed. Therefore, our system would work as an *electrically tunable, fully reversible valley filter* using tiny magnetic fields.

This is better seen in Fig. 3, where we plot the density distribution when electrons are injected from the source terminal (left side). The two valleys (Fig. 3a and Fig. 3b) contribute differently since the magnetic field is finite. While for valley K electrons impinge from the bottom left kink (Fig. 3a), the opposite valley K' electrons (Fig. 3b) enter from the top left kink. The former (latter) are mostly transmitted (reflected), giving rise to a valley polarized current in the drain terminal (right side).

The dependence of G on the constriction length L_x (see Fig. 4) further supports our interpretation. We display the conductance for $V_s^{(C)}$ corresponding to the four regions indicated in Fig. 2a. In the gapped region A the conductance decays exponentially for large values of L_x, which agrees with a transport mechanism based on tunnel effect. In regions B and D the conductance shows an oscillatory behavior up to arbitrarily large distances, implying a Fabry-Perot interference between propagating modes in the central area. The conductance becomes quantized at $4e^2/h$ in region C, which occurs when the interfaces between the leads and the constriction becomes transparent. Finally, in region D we recover the oscil-
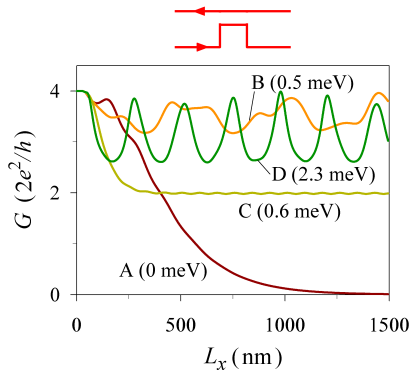
FIG. 4. Dependence of the conductance on the constriction length L_x for the results of Fig. 2a and selected values of $V_s^{(C)}$, as given in parenthesis. A-D labels are used to indicate the same regions of Fig. 2a.

latory behavior due to the activation of a new transport channel. In all cases the role of quantum tunneling for small L_x is clearly seen because the conductance increases as L_x shrinks to zero and scattering thus disappears.

B. Side loops

Let us turn to the loops created as the gate position y_0 shown in Fig. 1a increases. Then, the edge states in the central region detach as illustrated in Fig. 1c. Figure 5a shows in this case a conductance pattern that strongly differs from the wire system of Fig. 2a. G is characterized by resonant peaks that reach values of the order of $4e^2/h$ (we plot $G/2$ for convenience). Interestingly, these peaks are correlated with the discrete levels in the closed loop. To see this, we plot in Fig. 5d the loop energy spectrum. We find that the position of the conductance peaks agree, apart from a slight renormalization due to the coupling with to external edge states, with the level positions. The particular peak structure is highly sensitive to the loop dimensions (L_x, L_y) due to quantum confinement.

A small magnetic field splits the conductance peaks, as shown in Fig. 5b where we plot the valley resolved G for $B = 50$ mT. It is noticeable that the peak widths are significantly reduced in the presence of B, thus leading to smaller conductance minima; cf. Figs. 5a and 5c. The conductance splitting is explained with the level behavior as a function of B as shown in Fig. 5d. The field acts differently on the two valleys, thus raising (lowering) the energy for $\tau_z \to 1$ ($\tau_z \to -1$). B-splitting of the two valleys is also present for the case of non topological bound states in graphene circular quantum dots, discussed in Ref. 35, where states of the same angular momentum and opposite valleys show opposite dispersions at low fields. Besides the splitting, the spectrum in Fig.
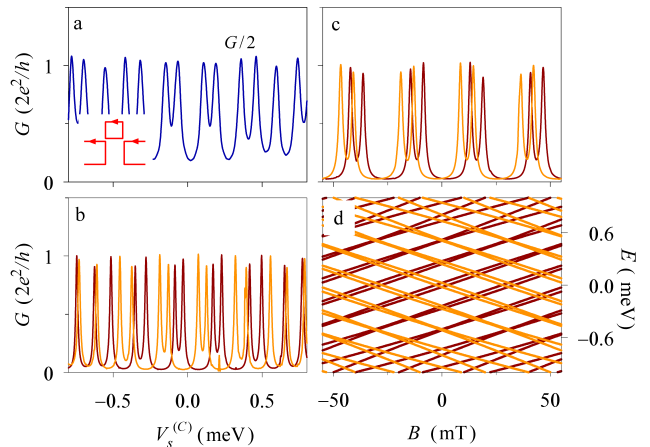

FIG. 5. Results for a side loop (inset in panel a) with $L_y = 150$ nm, $y_0 = 310$ nm and Fermi energy $E = 0.02$ meV. (a,b) Conductance for $L_x = 1\,\mu$m as a function of the central potential $V_s^{(C)}$ for $B = 0$ (a) and $B = 50$ mT (b). (c) Conductance as a function of the magnetic field for $V_s(C) = 0$. (d) Energy levels for the finite loop $(L_x, L_y) = (1\,\mu\text{m}, 150\,\text{nm})$ as a function of the field. The two colors in panels b-d indicate the two different valleys.

5d for topological loops shows a pattern of almost parallel lines for each valley, reflecting a quantization condition of the topological states along the perimeter of the loop[27]. Our results obey reciprocity, i.e., G is unchanged when both B and the valley index are simultaneously reversed, as can be seen in Fig. 5c. It is also worth stressing that the valley and gate sensitivity allows, as in the constriction, switching the valley polarization of the current by soley tuning the gate potential, only that a finer tuning is needed in the detached loop in order to hit the narrower peak maxima.

Probability density distributions in space provide a more visual support for this valley switch effect (see Fig. 6). We note that just one valley is populating the loop (Fig. 6b) while the other one is reflected (Fig. 6a). Thus, the valley-split resonant conductances of side loops in small magnetic fields imply high valley accumulations on the loop for specific gate potentials.

We now briefly discuss the dependence on L_x. In Fig. 7 we show results for a wide loop of $L_y = 150$ nm as in Fig. 5a. For $V_s^{(C)}$ corresponding to a conductance valley in Fig. 5a the conductance curve in Fig. 7a (black line) shows a single-mode regular spacing, which is in agreement with the degeneracy due to level crossing for $E = 0$ of Fig. 7b. In contrast, for a $V_s^{(C)}$ value that generates a G peak in Fig. 5a the conductance curve shows multiple-mode spacings in Fig. 7a (light green line). Further, we get accidental crossings at values of L_x that lead to additional factor-2 degeneracies in Fig. 7b. The case of a narrow loop ($L_y = 100$ nm) is shown in Fig. 8. In contrast to the previous case, the conductance valley
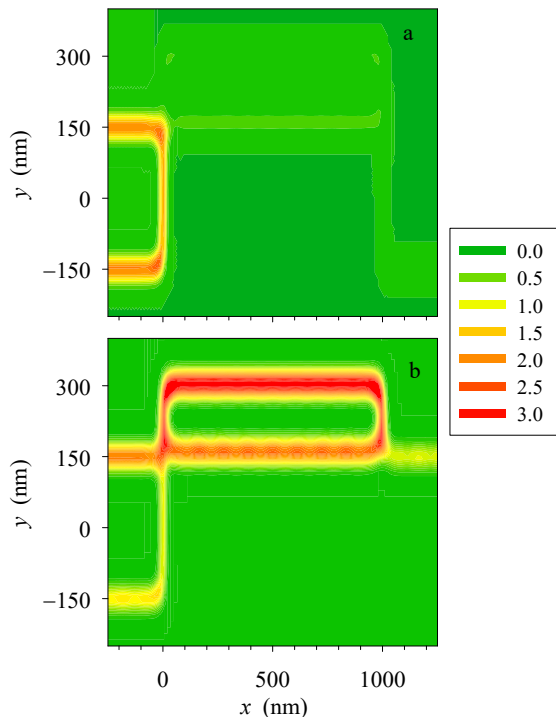
FIG. 6. Density distribution corresponding to the results of a side loop depicted in Fig. 5b. The central gate potential is $V_s^{(C)} = 0.3$ meV and it corresponds to a K' valley peak (light color) in Fig. 5b. Panels a and b are for the two different valleys K and K', respectively. Parameters: $L_x = 1000$ nm, $L_y = 150$ nm, $L_y' = 300$ nm, $y_0 = 310$ nm, $B = 50$ mT, $E = 0.02$ meV and $V_s^{(C)} = 0.3$ meV.
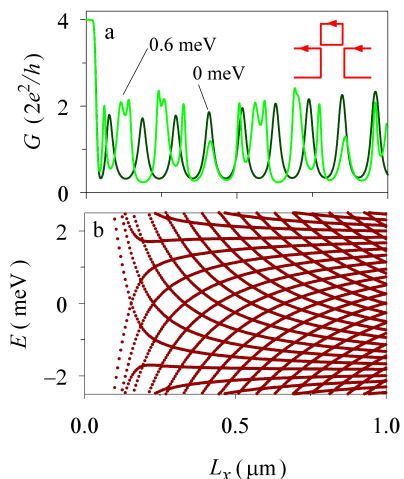

FIG. 7. (a) L_x dependence of the conductance for two selected values of $V_s^{(C)}$ for the parameters of the $L_y = 150$ nm side loop of Fig. 5a. (b) Energy levels of the closed rectangular loop with $L_y = 150$ nm as a function of L_x.
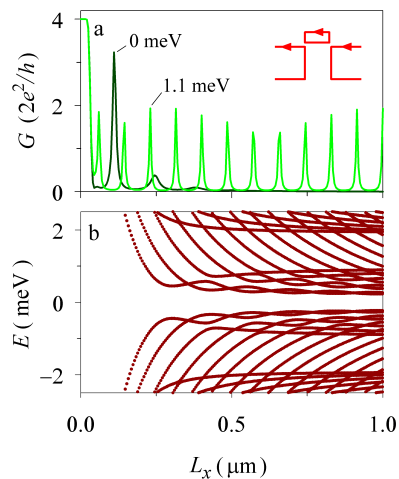

FIG. 8. (a) L_x dependence of the conductance for a narrow loop ($L_y = 100$ nm) and two selected values of $V_s^{(C)}$ with the rest of the parameters as in Fig. 7. (b) Energy levels of the closed loop with the same $L_y = 100$ nm as a function of L_x.

curve is quenched as L_x increases (black line in Fig. 8a) whereas the peak curve exhibits a beating pattern over-imposed to the peak sequence (green line). Figure 8b shows the energy levels when the narrow loop is closed. We observe regions with a bunching of levels separated from others with regularly spaced levels. This is consistent with the conductance peaks obtained in Fig. 8a. Despite the fact that the conductance patterns depend on the specific geometry of the loop (via L_x and L_y), in all cases the conductance peaks are correlated with the energy levels of the closed loop. Thus, the conductance serves as an excellent tool to probe the internal structure of topologically bound states.

IV. CONCLUSIONS

We have proposed a versatile nanodevice for topological studies in quantum valley transport. Transmission manipulation is achieved by means of a kink-antikink local potential that allows the formation of (i) point contacts with anomalous quantized conductance and (ii) side loops with chiral quasi-bound states. The obtained conductance curves provide information on the system energy spectrum. For tiny magnetic fields we obtain a valley polarization effect and this polarization is tunable with the gate potential.

These illustrative examples do not exhaust the capabilities of our system, where more sophisticated setups could be envisaged. Importantly, the predictions we make here will be unaffected by disorder in realistic samples since the device works at low energies with topological states only, which are robust against weak or moderate disorder strengths[36]. Finally, our model could be straight-
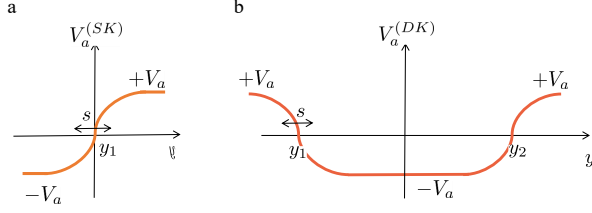
FIG. 9. Sketch of the smooth asymmetric potentials in (a) single kink and (b) double kink (also called kink-antikink in the main text). The diffusivity parameter s controls the degree of smoothness.

forwardly extended to multivalley materials other than bilayer graphene such as silicene[37], sonic crystals[38] and photonic platforms[39].

Appendix A: Potential smoothness

Smoothness in the space variation of the asymmetric potential $V_a(y)$ is described with a logistic function. A smooth step at position y_1 and diffusivity s (equivalently, the steepness inverse) is represented by

$$\mathcal{F}(y, y_1, s) = \frac{1}{1 + e^{(y-y_1)/s}} \ . \qquad \text{(A1)}$$

In detail, the case of a single kink at y_1 reads

$$V_a^{(sk)}(y) = V_a \left[1 - 2\mathcal{F}(y, y_1, s)\right] \ , \qquad \text{(A2)}$$

with the asymptotic values $V_a^{(sk)}(\pm\infty) = \pm V_a$. In a straightforward extension, the double kink forming a kink-antikink system at y_1 and y_2 reads

$$V_a^{(dk)}(y) = V_a \left[1 + 2\mathcal{F}(y, y_1, s) - 2\mathcal{F}(y, y_2, s)\right] \ , \qquad \text{(A3)}$$

Sketches of single and double kinks with the above parametrizations are shown in Fig. 9.

Appendix B: Kink-antikink gap

We address here how the gap of the kink-antinkink band structure (see Fig. 2b) varies with the separation L_y and the potential diffusivity s. The results are shown in Fig. 10a and b, respectively, and they confirm, as was anticipated, that the gap strongly increases when L_y decreases. However, it is remarkable that this dependence is non monotonic, with oscillations and with particular values of L_y and s for which the gap vanishes. This behavior can be attributed to the oscillations of the wave functions[16,17], as can be seen from the overlap of two displaced kink states

$$\mathcal{O}(L_y) = \left| \sum_{\sigma\tau\lambda} \int dy \ \psi^*_{\sigma\tau\lambda}(y) \, \psi_{\sigma\tau\lambda}(y - L_y) \right| \ , \qquad \text{(B1)}$$

shown in the inset to Fig. 10a. In Eq. (B1) ψ is the wave function for k near the branch crossing at zero energy of the single kink. For the steep potential in Fig. 10 ($s = 12$ nm) the L_y of minimum gap and the L_y of vanishing overlap are in good agreement, while for the smooth potential ($s = 40$ nm) the agreement is only qualitative.
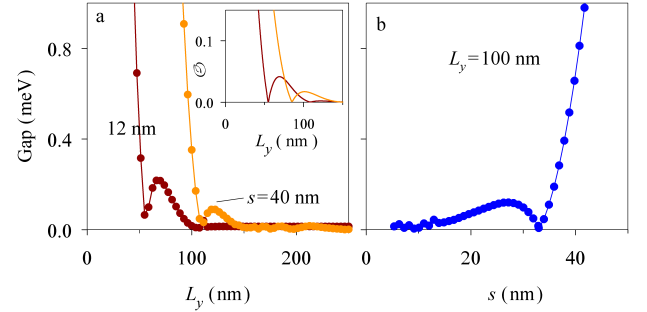

FIG. 10. a) Energy gap of the kink-antikink band structure as a function of the separation L_y and for two potential diffusivities s. The data points are obtained from the numerical band structure while the joining lines are a guide to the eye. The inset shows the wave function overlap $\mathcal{O}$ of independent kink and antinkink as a function of distance with the same color code. b) Energy gap as a function of the diffusivity for a fixed separation. Parameters: $V_a = 10$ meV, $V_s = 0$.

[1] Björn Trauzettel, Denis V. Bulaev, Daniel Loss, and Guido Burkard, "Spin qubits in graphene quantum dots," Nature Physics **3**, 192–196 (2007).

[2] J. Milton Pereira, P. Vasilopoulos, and F. M. Peeters, "Tunable quantum dots in bilayer graphene," Nano Letters **7**, 946–949 (2007).

[3] Patrik Recher and Björn Trauzettel, "Quantum dots and spin qubits in graphene," Nanotechnology **21**, 302001 (2010).

[4] Edward McCann and Mikito Koshino, "The electronic properties of bilayer graphene," Reports on Progress in Physics **76**, 056503 (2013).

[5] A.V. Rozhkov, A.O. Sboychakov, A.L. Rakhmanov, and Franco Nori, "Electronic properties of graphene-based bilayer systems," Physics Reports **648**, 1–104 (2016), electronic properties of graphene-based bilayer systems.

[6] Y. Zhang, T.-T. Tang, C. Girit, Z. Hao, M. C. Martin, A. Zettl, M. F. Crommie, Y. R. Shen, and F. Wang, "Direct observation of a widely tunable bandgap in bilayer graphene," Nature **459**, 820–823 (2009).

[7] Hiske Overweg, Hannah Eggimann, Xi Chen, Sergey Slizovskiy, Marius Eich, Riccardo Pisoni, Yongjin Lee, Peter Rickhaus, Kenji Watanabe, Takashi Taniguchi, Vladimir Fal'ko, Thomas Ihn, and Klaus Ensslin, "Electrostatically induced quantum point contacts in bilayer graphene," Nano Letters **18**, 553–559 (2018).

[8] Hiske Overweg, Angelika Knothe, Thomas Fabian, Lukas Linhart, Peter Rickhaus, Lucien Wernli, Kenji Watanabe, Takashi Taniguchi, David Sánchez, Joachim Burgdörfer, Florian Libisch, Vladimir I. Fal'ko, Klaus Ensslin, and Thomas Ihn, "Topologically nontrivial valley states in bilayer graphene quantum point contacts," Phys. Rev. Lett. **121**, 257702 (2018).

[9] R. Kraft, I. V. Krainov, V. Gall, A. P. Dmitriev, R. Krupke, I. V. Gornyi, and R. Danneau, "Valley subband splitting in bilayer graphene quantum point contacts," Phys. Rev. Lett. **121**, 257703 (2018).

[10] B. Terrés, L. A. Chizhova, F. Libisch, J. Peiro, D. Jörger, S. Engels, A. Girschik, K. Watanabe, T. Taniguchi, S. V. Rotking, and C. Stampfer, "Size quantization of dirac fermions in graphene constrictions," Nature Communications **7**, 11528 (2016).

[11] V. Clericò, J. A. Delgado-Notario, M. Saiz-Bretín, A. V. Malyshev, Y. M. Meziani, P. Hidalgo, B. Méndez, M. Amado, F. Domínguez-Adame, and E. Diez, "Quantum nanoconstrictions fabricated by cryo-etching in encapsulated graphene," Sci. Rep. **9**, 13572 (2019).

[12] Marius Eich, F. Herman, Riccardo Pisoni, Hiske Overweg, Annika Kurzmann, Yongjin Lee, Peter Rickhaus, Kenji Watanabe, Takashi Taniguchi, Manfred Sigrist, Thomas Ihn, and Klaus Ensslin, "Spin and valley states in gate-defined bilayer graphene quantum dots," Phys. Rev. X **8**, 031023 (2018).

[13] Annika Kurzmann, Hiske Overweg, Marius Eich, Alessia Pally, Peter Rickhaus, Riccardo Pisoni, Yongjin Lee, Kenji Watanabe, Takashi Taniguchi, Thomas Ihn, and Klaus Ensslin, "Charge detection in gate-defined bilayer graphene quantum dots," Nano Letters **19**, 5216–5221 (2019).

[14] L. Banszerus, A. Rothstein, T. Fabian, S. Möller, E. Icking, S. Trellenkamp, F. Lentz, D. Neumaier, K. Watanabe, T. Taniguchi, F. Libisch, C. Volk, and C. Stampfer, "Electron hole crossover in gate-controlled bilayer graphene quantum dots," Nano Letters **20**, 7709–7715 (2020).

[15] L. Banszerus, K. Hecker, E. Icking, S. Trellenkamp, F. Lentz, D. Neumaier, K. Watanabe, T. Taniguchi, C. Volk, and C. Stampfer, "Pulsed-gate spectroscopy of single-electron spin states in bilayer graphene quantum dots," Phys. Rev. B **103**, L081404 (2021).

[16] Ivar Martin, Ya. M. Blanter, and A. F. Morpurgo, "Topological confinement in bilayer graphene," Phys. Rev. Lett. **100**, 036804 (2008).

[17] M. Zarenia, J. M. Pereira, G. A. Farias, and F. M. Peeters, "Chiral states in bilayer graphene: Magnetic field dependence and gap opening," Phys. Rev. B **84**, 125451 (2011).

[18] Fan Zhang, Allan H. MacDonald, and Eugene J. Mele, "Valley chern numbers and boundary modes in gapped bilayer graphene," Proceedings of the National Academy of Sciences **110**, 10546–10551 (2013).

[19] Long Ju, Zhiwen Shi, Nityan Nair, Yinchuan Lv, Chenhao Jin, Jairo Velasco, Claudia Ojeda-Aristizabal, Hans A. Bechtel, Michael C. Martin, Alex Zettl, James Analytis, and Feng Wang, "Topological valley transport at bilayer graphene domain walls," Nature **520**, 650–655 (2015).

[20] Matthew Killi, Tzu-Chieh Wei, Ian Affleck, and Arun Paramekanti, "Tunable luttinger liquid physics in biased bilayer graphene," Phys. Rev. Lett. **104**, 216406 (2010).

[21] Matthew Killi, Si Wu, and Arun Paramekanti, "Band structures of bilayer graphene superlattices," Phys. Rev. Lett. **107**, 086801 (2011).

[22] Jing Li, Ke Wang, Kenton J. McFaul, Zachary Zern, Yafei Ren, Kenji Watanabe, Takashi Taniguchi, Zhenhua Qiao, and Jun Zhu, "Gate-controlled topological conducting channels in bilayer graphene," Nature Nanotechnology **11**, 1060–1065 (2016).

[23] H. Chen, P. Zhou, J. Liu, J. Qiao, B. Oezyilmaz, and J. Martin, "Gate controlled valley polarizer in bilayer graphene," Nature Communications **11**, 1202 (2020).

[24] Zhenhua Qiao, Jeil Jung, Qian Niu, and Allan H. MacDonald, "Electronic highways in bilayer graphene," Nano Letters **11**, 3453–3459 (2011).

[25] Jing Li, Rui-Xing Zhang, Zhenxi Yin, Jianxiao Zhang, Kenji Watanabe, Takashi Taniguchi, Chaoxing Liu, and Jun Zhu, "A valley valve and electron beam splitter," Science **362**, 1149–1152 (2018).

[26] Shu-guang Cheng, Haiwen Liu, Hua Jiang, Qing-Feng Sun, and X. C. Xie, "Manipulation and characterization of the valley-polarized topological kink states in graphene-based interferometers," Phys. Rev. Lett. **121**, 156801 (2018).

[27] L. J. P. Xavier, J. M. Pereira, Andrey Chaves, G. A. Farias, and F. M. Peeters, "Topological confinement in graphene bilayer quantum rings," Applied Physics Letters **96**, 212108 (2010).

[28] D.R. da Costa, M. Zarenia, Andrey Chaves, G.A. Farias, and F.M. Peeters, "Analytical study of the energy levels in bilayer graphene quantum dots," Carbon **78**, 392–400 (2014).

[29] Llorenç Serra, "Majorana modes and complex band structure of quantum wires," Phys. Rev. B **87**, 075440 (2013).

[30] Javier Osca and Llorenç Serra, "Complex band-structure analysis and topological physics of Majorana nanowires," Eur. Phys. J. B **92**, 101 (2019).

[31] R. B. Lehoucq, D. C. Sorensen, and C. Yang, *ARPACK Users Guide: Solution of Large-Scale Eigenvalue Problems with Implicitly Restarted Arnoldi Methods* (Philadelphia: SIAM. ISBN 978-0-89871-407-4, 1998).

[32] Leonard Susskind, "Lattice fermions," Phys. Rev. D **16**, 3031–3039 (1977).

[33] H.B. Nielsen and M. Ninomiya, "Absence of neutrinos on a lattice: (i). proof by homotopy theory," Nuclear Physics B **185**, 20–40 (1981).

[34] Alexis R. Hernández and Caio H. Lewenkopf, "Finite-difference method for transport of two-dimensional massless Dirac fermions in a ribbon geometry," Phys. Rev. B **86**, 155439 (2012).

[35] Patrik Recher, Johan Nilsson, Guido Burkard, and Björn Trauzettel, "Bound states and magnetic field induced valley splitting in gate-tunable graphene quantum dots," Phys. Rev. B **79**, 085407 (2009).

[36] Jian Li, Ivan Martin, Markus Büttiker, and Alberto F. Morpurgo, "Topological origin of subgap conductance in insulating bilayer graphene," Nature Phys. **7**, 38 (2011).

[37] Hui Pan, Zhenshan Li, Cheng-Cheng Liu, Guobao Zhu, Zhenhua Qiao, and Yugui Yao, "Valley-polarized quantum anomalous hall effect in silicene," Phys. Rev. Lett. **112**, 106802 (2014).

[38] Jiuyang Lu, Chunyin Qiu, Liping Ye, Xiying Fan, Manzhu Ke, Fan Zhang, and Zhengyou Liu, "Observation of topological valley transport of sound in sonic crystals," Nature Physics **13**, 369 (2017).

[39] Fei Gao, Haoran Xue, Zhaoju Yang, Kueifu Lai, Yang Yu, Xiao Lin, Yidong Chong, and Gennady Shvets, "Topologically protected refraction of robust kink states in valley photonic crystals," Nature Physics **14**, 140 (2017).